Interpolation of 2-D Vector Data Using Constraints from Elasticity

David T. Sandwell

Scripps Institution of Oceanography, UC San Diego, La Jolla, CA

Paul Wessel

SOEST, University of Hawaii at Mānoa, Honolulu, HI

Key points: interpolation of vector data, GPS gridding, Green's functions for 2-D elastic body

Abstract

We present a method for interpolation of sparse two-dimensional vector data. The method is based on the Green's functions of an elastic body subjected to in-plane forces. This approach ensures elastic coupling between the two components of the interpolation. Users may adjust the coupling by varying Poisson's ratio. Smoothing can be achieved by ignoring the smallest eigenvalues in the matrix solution for the strengths of the unknown body forces. We demonstrate the method using irregularly distributed GPS velocities from southern California. Our technique has been implemented in both GMT and MATLAB®.

Introduction

Interpolation of randomly located scalar data onto a uniform grid is commonly performed using the finite-difference, multigrid, minimum curvature method [*Briggs,* 1974; *Swain,* 1976; *Smith and Wessel,* 1990] or the direct biharmonic spline method [*Sandwell,* 1987; *Wessel and Bercovici,* 1998]. The multigrid minimum curvature approach is extremely efficient and can handle large data sets of perhaps a billion data points, but suffers from slow numerical convergence. The direct biharmonic spline approach is more flexible and can interpolate data with differing uncertainties but is limited to only a few thousand points because an *N*-data by *N*-data matrix inversion is required. Moreover, the inversion usually requires some numerical stabilization to achieve a smooth result. The basic approach is to apply vertical point loads to a thin elastic sheet at the locations of the data constraints. The

36   strengths of these forces are then adjusted through a least squares inversion such that the
37   deformed sheet matches the data points within their uncertainties. Then the deformation, or
38   its derivatives, can be calculated anywhere within the boundaries of the data. The Green's
39   function for the response of a thin elastic sheet to a point load at (x_o, y_o) is simply

40    $\phi(\vec{r}) = r^2\left[\ln(r) - 1\right]$ where $\vec{r} = (x - x_o, y - y_o)$ [*Sandwell*, 1987]. *Wessel and Bercovici* [1998]

41   extended the method to include in-plane tension, which damps the undesirable overshoots of
42   the elastic sheet. In this case the Green's function is slightly more complicated, i.e.,

43    $\phi(\vec{r}) = K_o(pr) + \ln(pr)$, where K_o is the zero order, modified Bessel function of the second

44   kind and p is related to the prescribed tension factor.
45   Here we investigate a similar Green's function approach for interpolation of 2-D vector
46   data. This is not a new idea. *Haines et al.*, [1993, 2015] proposed using a 2-D elastic model
47   to provide coupling between the two horizontal velocity components of GPS models. The
48   basic approach is similar to the biharmonic spline interpolation approach. One imposes
49   vector forces at the data locations. These forces deform the elastic body, resulting in a vector
50   deformation field. The strengths of the force vectors are adjusted until velocities match the
51   vector data. *Haines et al.*, [2015] used a finite element modeling approach where element
52   nodes are placed at the data locations to compute the Green's functions and then used a least-
53   squares approach to adjust the forces to match the data. Here we replace the finite element
54   computations with analytic Green's functions for the in-plane response of a 2-D elastic body
55   to in-plane forces. This greatly simplifies the computations and allows for the analytic
56   calculation of deformation gradients (i.e., the strain tensor). Moreover, by adjusting
57   Poisson's ratio the strain field can be tuned to extremes such as incompressible (1.0), typical
58   elastic (0.5) or even a value of -1 that basically removes the elastic coupling of vector
59   interpolation.
60
61   *Green's Functions*

62   We wish to calculate the 2-D displacement vector $\vec{u}(x,y) = u(x,y)\hat{i} + v(x,y)\hat{j}$ due to a 2-

63   D vector in-plane body force. *Haines et al.*, [2015] developed the quasi-static force balance
64   equations in 2-D as
65

$$\left(\frac{2}{1-v}\right)\frac{\partial^2 u}{\partial x^2}+\left(\frac{2v}{1-v}\right)\frac{\partial^2 v}{\partial x \partial y}+\frac{\partial^2 u}{\partial y^2}+\frac{\partial^2 v}{\partial x \partial y}=\frac{-f_x}{\mu}\delta(x)\delta(y)$$

$$\frac{\partial^2 u}{\partial x \partial y}+\frac{\partial^2 v}{\partial x^2}+\left(\frac{2v}{1-v}\right)\frac{\partial^2 u}{\partial x \partial y}+\left(\frac{2}{1-v}\right)\frac{\partial^2 v}{\partial y^2}=\frac{-f_y}{\mu}\delta(x)\delta(y)$$

(1)

where v is Poisson's ratio, μ is the shear modulus, and $\left(f_x, f_y\right)$ is the force vector. The units are force per distance and forces are applied at a point using the 2-D delta function $\delta(x)\delta(y)$. This problem is most easily solved by taking the 2-D Fourier transform of (1). The transformed equations become

$$\begin{bmatrix}\left(\dfrac{2}{1-v}\right)k_x^2+k_y^2 & \left(\dfrac{1+v}{1-v}\right)k_x k_y \\ \left(\dfrac{1+v}{1-v}\right)k_x k_y & \left(\dfrac{2}{1-v}\right)k_y^2+k_x^2\end{bmatrix}\begin{bmatrix}U(\vec{k}) \\ V(\vec{k})\end{bmatrix}=\frac{1}{4\pi^2\mu}\begin{bmatrix}f_x \\ f_y\end{bmatrix}.$$

(2)

where k_x and k_y are wavenumbers (1/wavelength). To determine the response from a point force we need to invert this set of equations and take the inverse 2-D Fourier transform of the result. The matrix inverse is

$$\begin{bmatrix}U(\vec{k}) \\ V(\vec{k})\end{bmatrix}=\frac{1}{8\pi^2\mu k_r^4}\begin{bmatrix}2k_r^2-(1+v)k_x^2 & -(1+v)k_x k_y \\ -(1+v)k_x k_y & 2k_r^2-(1+v)k_y^2\end{bmatrix}\begin{bmatrix}f_x \\ f_y\end{bmatrix}$$

(3)

where $k_r^2 = k_x^2 + k_y^2$. Note that in the special case of a Poisson's ratio of -1 the solution simplifies to

$$\begin{bmatrix}U(\vec{k}) \\ V(\vec{k})\end{bmatrix}=\frac{1}{4\pi^2\mu k_r^2}\begin{bmatrix}1 & 0 \\ 0 & 1\end{bmatrix}\begin{bmatrix}f_x \\ f_y\end{bmatrix}$$

(4)

85

86 This corresponds to interpolation with no coupling between the two velocity components and

87 the Green's function is simply $\phi(\vec{r}) = \ln r$. Here, the two components of GPS velocities

88 would be decoupled and interpolated separately. The general solution depends on three

89 functions in equation 3:

90

91 $$Q(\vec{k}) = \frac{2k_r^2 - (1+v)k_x^2}{k_r^4}, \quad P(\vec{k}) = \frac{2k_r^2 - (1+v)k_y^2}{k_r^4}, \quad W(\vec{k}) = \frac{-(1+v)k_x k_y}{k_r^4}. \tag{5}$$

92

93 To obtain the space domain solution we will need to evaluate the 2-D inverse Fourier

94 transform of the following four component functions:

95

96 $$\mathfrak{I}_2^{-1}\left[\frac{1}{k_x^2 + k_y^2}\right], \quad \mathfrak{I}_2^{-1}\left[\frac{k_x^2}{\left(k_x^2 + k_y^2\right)^2}\right], \quad \mathfrak{I}_2^{-1}\left[\frac{k_y^2}{\left(k_x^2 + k_y^2\right)^2}\right], \quad \mathfrak{I}_2^{-1}\left[\frac{k_x k_y}{\left(k_x^2 + k_y^2\right)^2}\right]. \tag{6}$$

97

98 The inverse transforms of these four functions are straightforward and yield

99

100 $$-\ln r, \quad \frac{1}{2}\left[\frac{y^2}{r^2} - \ln r\right], \quad \frac{1}{2}\left[\frac{x^2}{r^2} - \ln r\right], \quad -\frac{1}{2}\frac{xy}{r^2}. \tag{7}$$

101

102 In the space domain the three Green's functions given by (5) can be written as

$$q(\vec{r}) = 4\ln r + (1+v)\left(\frac{y^2}{r^2} - \ln r\right) = (3-v)\ln r + (1+v)\frac{y^2}{r^2}$$

103 $$p(\vec{r}) = (3-v)\ln r + (1+v)\frac{x^2}{r^2} \tag{8}$$

$$w(\vec{r}) = -(1+v)\frac{xy}{r^2}.$$

104 We checked the Green's functions by showing they solve the original differential equation

105 (1). This was accomplished using the computer algebra capabilities in MATLAB.

106   A description of the numerical approach follows. We wish to compute a smooth vector
107 velocity field that matches a finite set of N measured vectors $u(\vec{r}_i), v(\vec{r}_i)$, where $\vec{r}_i = (x_i, y_i)$
108 are the locations of the vectors. This is accomplished by solving for a set of N vector body
109 forces f_x^j, f_y^j that are applied at the locations of the velocity measurements. To determine the
110 strength of the body forces we invert the following $2N$ by $2N$ linear system of equations:
111

112
$$\begin{bmatrix} u(\vec{r}_i) \\ v(\vec{r}_i) \end{bmatrix} = \begin{bmatrix} q(\vec{r}_i - \vec{r}_j) & w(\vec{r}_i - \vec{r}_j) \\ w(\vec{r}_i - \vec{r}_j) & p(\vec{r}_i - \vec{r}_j) \end{bmatrix} \begin{bmatrix} f_x^j \\ f_y^j \end{bmatrix}$$
(9)

113
114 Finally, the vector velocity field can be computed at any location using
115

116
$$u(\vec{r}) = \sum_{j=1}^{N} \left[q(\vec{r} - \vec{r}_j) f_x^j + w(\vec{r} - \vec{r}_j) f_y^j \right]$$
$$v(\vec{r}) = \sum_{j=1}^{N} \left[w(\vec{r} - \vec{r}_j) f_x^j + p(\vec{r} - \vec{r}_j) f_y^j \right]$$
(10)

117
118 We have implemented this approach as a new module *gpsgridder* to the Generic Mapping
119 Tools (GMT) [*Wessel et al.*, 2013]. The $2N$ by $2N$ matrix in equation 9 can be solved in a
120 variety of ways. For the *gpsgridder* implementation we use the singular value
121 decomposition algorithm implemented in LAPACK. The user can decide to keep all the
122 singular values (solved by LU decomposition) or a subset which results in some smoothing
123 of the solution. Starting at GMT release 5.3.0, the new module can be found in the
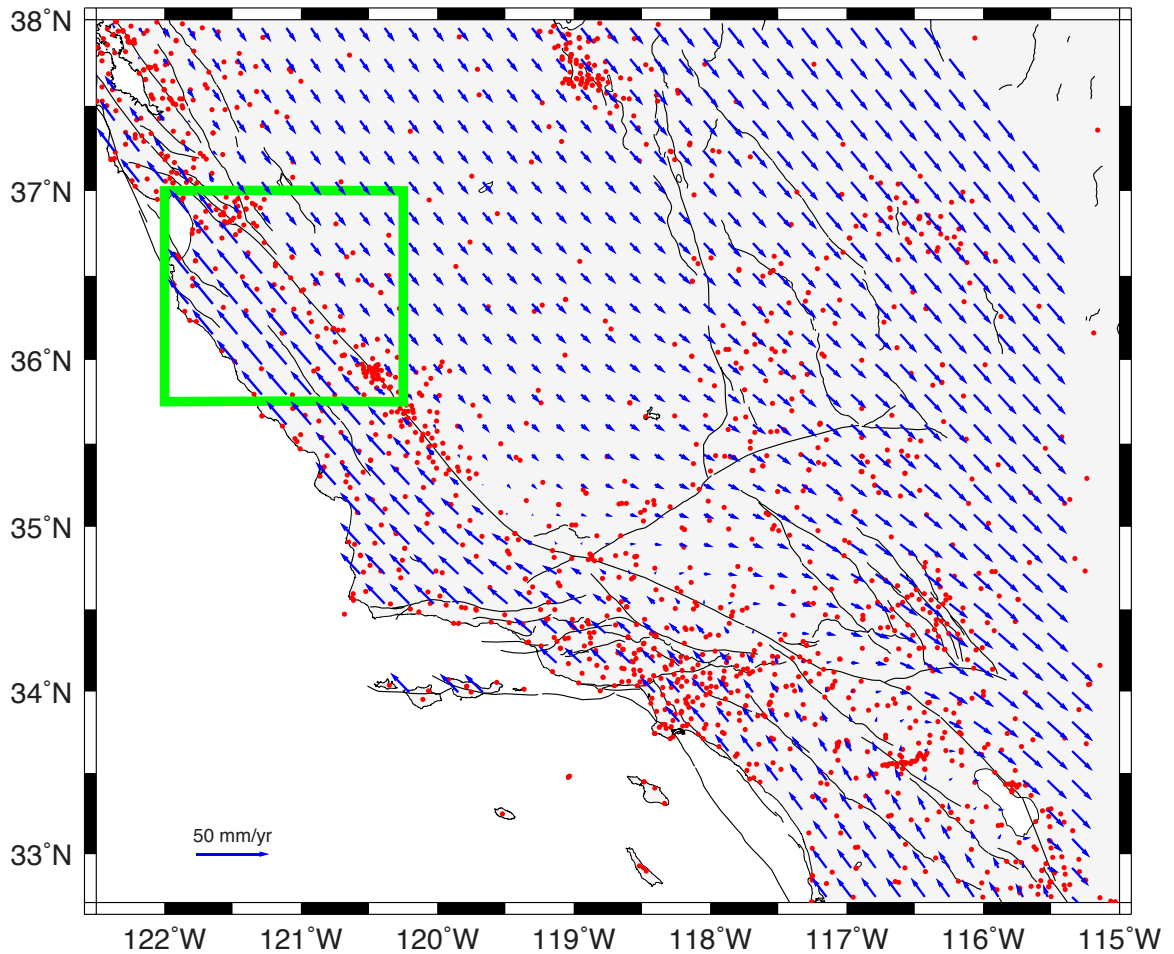124 supplemental "potential" package.
125
126 *Application to GPS data*
127   The 2-D velocity field derived from surface geodetic measurements is an important
128 quantity used to measure strain localization above locked faults as well as strain
129 accumulation in the interiors of crustal blocks. Faults that have a shallow locking will
130 require spatial resolution of 2-3 km [*Smith and Sandwell*, 2003]. However, the typical
131 spacing of GPS points in California is ~9 km [*Wei et al.*, 2010] so the strain-rate field is not
132 completely resolved by the GPS data. Currently there are several approaches to mapping
133 strain rate from vector GPS data. The most accurate approaches make assumptions about the

134 locations, slip rates, and locking depths of the major faults [*Hearn et al.*, 2010]. These are

135 typically based on block models. The models sometimes have a uniform strain in the block

136 interiors to absorb the residual velocity not captured by the locked dislocations [*McCaffrey et*

137 *al.*, 2013]. Another approach is to make no assumptions about the fault structure and simply

138 do a biharmonic interpolation of each velocity component independently [*Hackl et al.*,

139 2009]. However this leads to suboptimal results. A distance-weighted, least-squares

140 approach, recently developed by *Shen et al.*, [2015], provides an improved strain-rate map

141 without using a priori information about fault locations and orientations. The interpolation

142 approach developed in *Haines et al.*, [1993, 2015] provides coupling between the two

143 horizontal velocity components, resulting in a more accurate interpolation of the velocity and

144 strain field.

145   To illustrate the benefits of the coupled interpolation in relation to the biharmonic spline

146 approach we begin with a realistic model for the vector velocity field for a large region

147 surrounding the San Andreas Fault system [*Tong et al.*, 2013; 2014]. The velocity model is

148 based on 1981 GPS velocity vectors as well as higher spatial resolution line-of-sight velocity

149 measurements from ALOS-1 radar interferometry. The slip rates and locking depths along

150 41 fault segments are adjusted to match all the velocity data (Figure 1). This model results in

151 north and east grids of velocity at 1 km spacing. A prominent feature of the model is a

152 creeping section of the San Andreas Fault system where there is an abrupt change in velocity

153 across the fault (Figure 1 – green box). We sample the two components of velocity at 1768

154 unique locations (Figure 1 – red dots) resulting in 3536 observations. We then use the

155 biharmonic and coupled methods to interpolate over the areas of adequate data coverage and

156 compare the interpolated velocity and strain rate grids with the "known" velocity and strain

157 rates. The biharmonic and coupled approaches are implemented in GMT as *greenspline* and

158 *gpsgridder*, respectively. Each program has a number of parameters that can be adjusted to

159 achieve an optimal fit. The *greenspline* approach achieves the best fit for zero tension factor,

160 which corresponds to biharmonic spline interpolation [*Sandwell,* 1984]. The *gpsgridder*

161 approach has two main parameter adjustments. The first is a minimum radius factor that

162 needs to be added to all radial differences in equations (9) and (10) to keep the Green's

163 functions from becoming singular. After some trial and error, we found that a minimum

164 radius of 8 km provides the best overall fit to the data; this also roughly corresponds to the

165 mean spacing of the GPS points of ~9 km [*Wei et al.*, 2010]. The second parameter is the

166 value of Poisson's ratio used for the interpolation. We tested a range from -1 (fully

167 decoupled) to 0.5 (elastic) to 1.0 (incompressible). The results, provided in Table 1, show the

168 rms misfit of the interpolated velocity and strain rate grids with respect to the starting model.

169 We also performed the statistics for the interpolation over just the creeping section (bold in

170   Table 1). The rms misfits for this creeping area are larger than the rms misfits for the entire

171   area although the optimal minimum radius is also 8 km.

172

173   Figure 1. Velocity vectors over a large area surrounding the San Andreas Fault system based

174   on an earthquake cycle model [*Tong et al.*, 2013; 2014]. The total change in velocity across

175   the fault system is 45 mm/yr. The red dots show locations of the GPS velocity measurements

176   used to construct this model. We sample the model at these locations and then use various

177   interpolation methods to re-estimate the model. The green box shows the sharp velocity

178   change across the creeping section. These results are highlighted in Figure 2.

179

180

181 Table 1.

model	Poisson's ratio	minimum radius (km)	rms misfit				
			u mm/yr	v mm/yr	e_{xx} 10^{-8}/yr	e_{xy} 10^{-8}/yr	e_{yy} 10^{-8}/yr
biharmonic	-	-	0.229	0.279	3.89	1.99	4.16
(un)coupled	-1.0	8	0.186	0.223	3.48	1.99	3.83
coupled	.0	8	0.165	0.190	2.90	1.82	3.12
"	.5	8	0.162	0.171	2.66	1.82	2.81
"	1.0	8	0.863	0.894	4.91	4.29	4.89
"	.5	0	-	-	-	-	-
"	.5	2	0.281/**0.710**	0.306/**0.903**	3.77	2.38	3.87
"	.5	4	0.215/**0.509**	0.232/**0.637**	3.11	2.08	3.22
"	.5	8	0.162/**0.432**	0.171/**0.450**	2.66	1.82	2.81
"	.5	12	0.182/**0.583**	0.188/**0.577**	3.05	2.16	3.21

182 Optimal model parameters are highlighted in blue. Bold are rms misfit for just the creeping
183 section shown in Figure 2.
184

185   The results for three of the most interesting cases are shown in Figure 2 where we have
186 zoomed in on the creeping section of the fault where the interpolation is most challenging.
187 Figure 2a shows velocity vectors from the *Tong et al.,* [2014] model. The vectors are
188 parallel to the fault and have relatively uniform length along the fault, although the direction
189 of the vectors reverses abruptly at the fault. The first example (Figure 2b) corresponds to the
190 biharmonic interpolation method where the east and north components of the vector velocity
191 are interpolated independently. The residual velocity field shows large spatial scale
192 variations in strength that results from the overshoot of the biharmonic spline. This
193 scalloping results in a relatively large misfit for both the velocity and strain rate components.
194 The second interpolation example (Figure 2c) corresponds to interpolation where the
195 Poisson's ratio is -1.0. This parameter selection results in no coupling between the east and
196 north components and the residuals are similar to the biharmonic case although somewhat
197 smaller. The last example (Figure 2d) is the coupled interpolation with a Poisson's ratio of
198 0.5. The residuals are significantly smaller and show more of a random orientation reflecting
199 the coupling between the two velocity components. This case also has a much smaller misfit
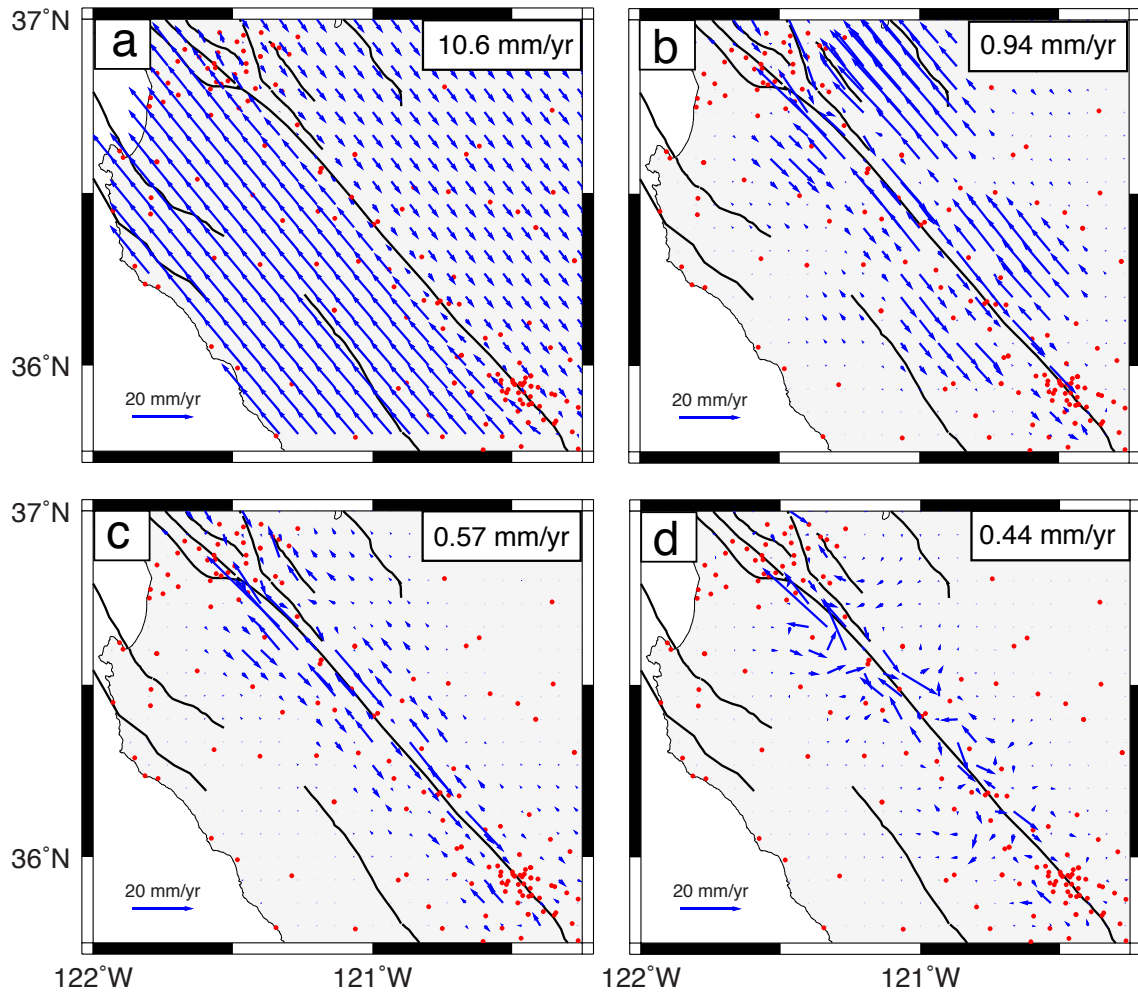200 in both velocity and strain rate than the two uncoupled cases.
201

Figure 2. Velocity vectors across the creeping section of the San Andreas Fault. (a) Original *Tong et al.*, [2014] model has an rms variation of 10.6 mm/yr. (b) Residual model based on biharmonic spline interpolation has an rms error of 0.94 mm/yr. (c) Residual model based on the coupled interpolation with a Poisson's ratio of -1 (no coupling between east and north velocity) has an rms error of 0.57 mm/yr. (d) Residual model based on the coupled interpolation with a Poisson's ratio of 0.5 has an rms error of 0.44 mm/yr.

One of the main applications of this method is to calculate a grid of strain rate from randomly distributed vector velocity measurements. Our analysis provides an estimate of the type of errors to expect in the second invariant of the strain rate when it is undersampled using the GPS station distribution provided in Figure 1. The original velocity model results in the strain rates shown in Figure 3a where there are areas of very high strain rate above faults that are creeping or have shallow locking depth (e.g. red areas > 500 nanostrain/yr). The model also has very low strain rate in the interiors of the blocks (e.g. blue areas < 10

217   nanostrain/yr). The difference between the original and recovered strain rate tensor converted
218   to second invariant are shown in Figure 3b. Errors are small (< 3 nanostrain/yr) in areas that
219   have adequate GPS sampling (white dots) and where the model strain rate is also small.
220   Errors are large (100 – 1000 nanostrain/yr) in areas where the model strain rate is large and
221   the GPS sampling is inadequate. To illustrate a couple of cases, the red arrow points to a
222   region of high strain rate where there is also dense GPS coverage. The strain rate error in
223   this area is quite low because of the good GPS coverage. In contrast the blue arrow points to
224   a region of high strain rate where there is sparse GPS coverage. The strain rate error in this
225   area is quite high because of the poor GPS coverage. Indeed this interpolation tool could be
226   used, along with a reasonable strain rate grid, to estimate the improvement in strain rate
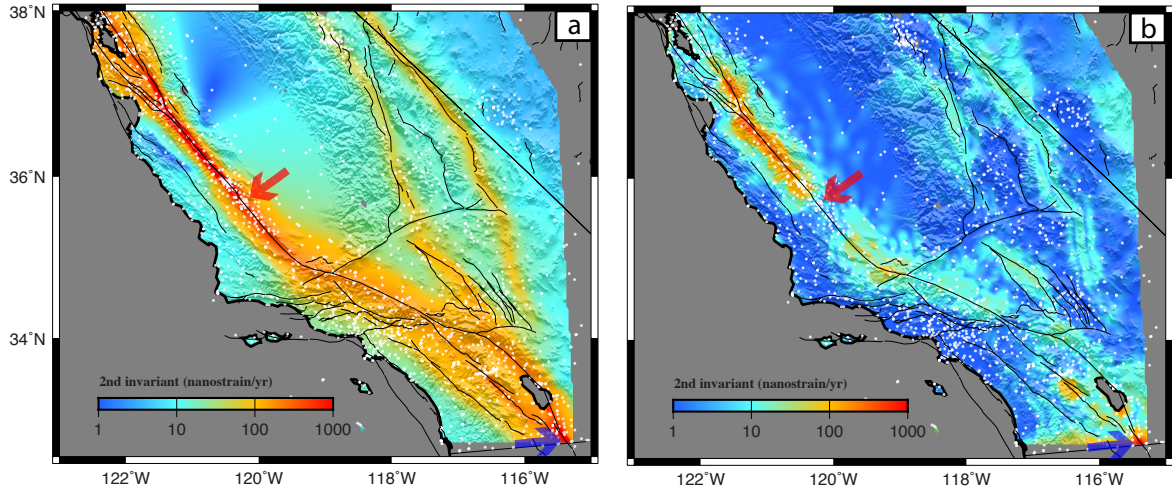227   accuracy for a prescribed GPS or InSAR data coverage.

228

229

230   Figure 3 (a) Second invariant of 2-D strain tensor $\varepsilon_{II} = \left(\varepsilon_{xx}^2 + \varepsilon_{yy}^2 + 2\varepsilon_{xy}^2 \right)^{1/2}$ derived from the
231   *Tong et al*., [2014] velocity grid. (b) Second invariant of the difference between the model
232   strain rate tensor and the strain rate tensor derived from the *gpsgridder* program with a
233   Poisson ratio of 0.5.

234

235   *Discussion and Conclusions*
236   While this method is not new, our analytic approach provides some insight into the
237   behavior of the coupled interpolation for a wide range of Poisson's ratio. As discussed in
238   *Haines et al*., [1993, 2015] this approach provides improved interpolation of sparse vector
239   data when the physics of the deforming material follows elasticity equations. There are other
240   attributes of this approach that have not been fully discussed in the paper although they will
241   be important for interpolation of noisy data. The first is the inversion of the set of linear

242 equations in (9) will be numerically unstable if the ratio of the largest to smallest spacing of
243 vector positions becomes too great. The *gpsgridder* program automatically eliminates
244 duplicate locations that would make the inversion exactly singular. In addition, the
245 *blockmedian* program can be used to combine nearby measurements. The second obvious
246 attribute not discussed above is that uncertainties are easily added to this formulation by
247 dividing both sides of equation (9) by the standard deviations of the data. This extension is
248 implemented in the *gpsgridder* program via the –C, –W options where the rms misfit of the
249 model to the noisy data can be adjusted by reducing the number of eigenvalues to use for the
250 singular value decomposition of the inversion. In the case above there were 3563
251 observations but tests where the number of eigenvalues was reduced to 2400 provided almost
252 identical uncertainties. We have found that an adequate fit to real GPS data is obtained when
253 the number of eigenvalues is ¼ the number of data points. The user will need to experiment
254 with these paramters to find acceptable solutions to fitting the data within the uncertainties.

255   One other important issue not discussed here is that this approach can only interpolate
256 thousands and not millions of data because of finite computer memory, computer precision
257 and computer time. A practical solution to dealing with very large data sets is to assemble
258 the data into finite size rectangular grids having 50% overlap. Data within each full subgrid
259 are used to solve for the vector forces but the vector model velocity is only computed in the
260 interior of each subgrid [e.g., *Sandwell,* 1987]. One final issue is that a variety of data types
261 such as GPS vectors and 2-D tensor strain measurements could be combined in the inversion.
262 This would require an extension of (9) to include analytical derivatives of Green functions,
263 which are messy but not difficult.

264   We have implemented this method in both GMT and MATLAB and provide example data
265 sets and programming parameters at the following ftp site
266 (ftp://topex.ucsd.edu/pub/sandwell/strain/gpsgridder_tests.tar)

267

276

References

278 Briggs, I. C. (1974), Machine contouring using minimum curvature, *Geophysics*, *39*(1), 39–
279   48.

280 Gradshteyn, I. S., and I. M. Ryzhik (1980), *Table of Integrals, Series, and Products*, 4th ed.,
281   Academic Press, San Diego, CA.
282 Hackl, M., R. Malservaisi, and S. Wdowinski (2009), Strain pattern from dense GPS
283   networks, *Nat. Hazards Earth Syst.*, 9., 1177-1187.
284 Haines, A. J., and W. E. Holt (1993), A procedure for obtaining the complete horizontal
285   motions within zones of distributed deformation from the inversion of strain rate data, *J.*
286   *Geophys. Res.*, *98*, 12,057–12,082.
287 Haines, A. J., L. L. Dimitrova, L. M. Wallace, and C. A. Williams (2015), *Enhanced Surface*
288   *Imaging of Crustal Deformation: Obtaining Tectonic Force Fields Using GPS Data*, 99
289   pp., Springer International Publishing, doi:10.1007/978-3-319-21578-5.
290 Hearn, E., K. Johnson, D. Sandwell, and W. Thatcher (2010), SCEC UCERF workshop
291   report: http://www.scec.org/workshops/2010/gps-ucerf3/FinalReport_GPS-
292   UCERF3Workshop.pdf,.
293 McCaffrey, R., King, R. W., Payne, S. J., & Lancaster, M. (2013). Active tectonics of
294   northwestern US inferred from GPS-derived surface velocities. Journal of Geophysical
295   Research: Solid Earth, 118(2), 709-723.
296 Sandwell, D. T. (1987), Biharmonic spline interpolation of Geos-3 and Seasat altimeter data,
297   *Geophys. Res. Lett.*, *14*(2), 139–142.
298 Shen, Z-K, M. Wang, Y. Zeng, and F. Wang, (2015) Optimal Interpolation of Spatially
299   Discretized Geodetic Data, *Bulletin of the Seismological Society of America, 105*, 4,
300   2117–2127, , doi: 10.1785/0120140247
301 Smith, W. H. F., and P. Wessel (1990), Gridding with continuous curvature splines in
302   tension, *Geophysics*, *55*(3), 293–305, doi:10.1190/1.1442837.
303 Smith, B., and D. Sandwell (2003), Coulomb stress accumulation along the San Andreas
304   Fault system, J. Geophys. Res., 108(B6), 2296, doi:10.1029/ 2002JB002136.
305 Swain, C. J. (1976), A FORTRAN IV program for interpolating irregularly spaced data using
306   the difference equations for minimum curvature, *Comput. & Geosci.*, *1*(4), 231-240.
307 Tong, X., D. T. Sandwell, and B. Smith-Konter (2013), High-resolution interseismic velocity
308   data along the San Andreas Fault from GPS and InSAR, J. Geophys. Res.; Solid Earth,
309   118, doi:10.1029/2012JB009442.
310 Tong, X., B. Smith-Konter, and D. T. Sandwell (2014), Is there a discrepancy between
311   geological and geodetic slip rates along the San Andreas Fault System?, *J. Geophys. Res.*
312   *Solid Earth, 119*, doi:10.1002/2013JB010765.
313 Wei, M., D. T. Sandwell, and B. Smith-Konter, Optimal combination of InSAR and GPS for
314   measuring interseismic crustal deformation, *J. Adv. in Space Res.*
315   doi:10.1016/j.asr.2010.03.013, 2010.
316 Wessel, P., and D. Bercovici (1998), Interpolation with splines in tension: a Green's function
317   approach, *Math. Geol.*, *30*(1), 77–93, doi:10.1023/A:1021713421882.
318 Wessel, P., W. H. F. Smith, R. Scharroo, J. F. Luis, and F. Wobbe (2013), Generic Mapping
319   Tools: Improved version released, *Eos Trans. AGU*, *94*(45), 409–410,
320   doi:10.1002/2013EO450001.
321